

Evidence for nonlinear reflections in shock-containing noise near high-performance military aircraft

Aaron B. Vaughn, Kevin M. Leete, Kent L. Gee, Bradley R. Adams, and J. Micah Downing

Citation: *The Journal of the Acoustical Society of America* **149**, 2403 (2021); doi: 10.1121/10.0003932

View online: <https://doi.org/10.1121/10.0003932>

View Table of Contents: <https://asa.scitation.org/toc/jas/149/4>

Published by the [Acoustical Society of America](#)

ARTICLES YOU MAY BE INTERESTED IN

[Characterization of topographic effects on sonic boom reflection by resolution of the Euler equations](#)

The Journal of the Acoustical Society of America **149**, 2437 (2021); <https://doi.org/10.1121/10.0003816>

[Atmospheric sound propagation in a stratified moving media: Application of the semi analytic finite element method](#)

The Journal of the Acoustical Society of America **148**, 3737 (2020); <https://doi.org/10.1121/10.0002912>

[Allan Pierce and adiabatic normal modes](#)

The Journal of the Acoustical Society of America **149**, R5 (2021); <https://doi.org/10.1121/10.0003595>

[Insertion loss of regular finite cylinder arrays with porous layers between the rows](#)

The Journal of the Acoustical Society of America **149**, 2395 (2021); <https://doi.org/10.1121/10.0004131>

[Numerical investigations of anisotropic structures of red blood cell aggregates on ultrasonic backscattering](#)

The Journal of the Acoustical Society of America **149**, 2415 (2021); <https://doi.org/10.1121/10.0003815>

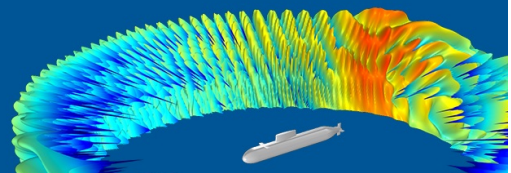
[Multi-sensor integration for an assessment of underwater radiated noise from common vessels in San Francisco Bay](#)

The Journal of the Acoustical Society of America **149**, 2451 (2021); <https://doi.org/10.1121/10.0003963>

COMSOL Day
Acoustics

A free, online event where you can attend
multiphysics simulation sessions, ask
COMSOL staff your questions, and more

JOIN US MAY 25 »



Evidence for nonlinear reflections in shock-containing noise near high-performance military aircraft^{a)}

Aaron B. Vaughn,^{1,b)} Kevin M. Leete,^{1,c)} Kent L. Gee,^{1,d)} Bradley R. Adams,² and J. Micah Downing^{3,e)}

¹Department of Physics and Astronomy, Brigham Young University, Provo, Utah 84602, USA

²Department of Mechanical Engineering, Brigham Young University, Provo, Utah 84602, USA

³Blue Ridge Research and Consulting, LLC, 29 North Market Street, Suite 700, Asheville, North Carolina 28801, USA

ABSTRACT:

Skewness values for the pressure time derivative are greater at ground-based measurements near a tactical aircraft than they are at nearby off-ground locations. A possible explanation for this phenomenon is the occurrence of nonlinear, irregular shock reflections at the ground. Propagation angle, source location, and corresponding angle of incidence relative to the ground are estimated using a two-point cross correlation of windowed shock events. Nonlinear reflections are likely to occur based on the combination of angles of incidence and measured shock strengths and cause a pressure increase at the shock that is greater than twice the free-field pressure. The associated pressure increase at the shocks appears to enhance shock-related metrics at the ground compared to off-ground locations.

<https://doi.org/10.1121/10.0003932>

(Received 12 October 2020; revised 5 February 2021; accepted 7 March 2021; published online 7 April 2021)

[Editor: James F. Lynch]

Pages: 2403–2414

I. INTRODUCTION

This study investigates the possibility and implications of nonlinear shock reflections in jet noise produced by a high-performance military aircraft. Acoustic shocks are characterized by abrupt changes of properties in the medium such as pressure, temperature, and density. In jet noise, shocks are intermittent events embedded within other jet noise components, occurring particularly in the loud, aft radiation region. Shocks have been shown to be present in the near field^{1,2} as well as in the far field,^{3,4} although far-field shocks are augmented due to nonlinear propagation.⁵ The reception of acoustic shocks is responsible for the perception of jet crackle,⁶ which is as an annoying⁷ and dominant⁸ component of supersonic jet noise. The skewness of the time derivative of the pressure waveform, $Sk\{\partial p/\partial t\}$ (hereafter referred to as the “derivative skewness”), is a metric indicative of crackle being perceived in jet noise⁹ as it is sensitive to the presence of acoustic shocks in the jet noise waveform.³ Of interest in this study is how ground reflections impact shocks in jet noise and the subsequently measured $Sk\{\partial p/\partial t\}$ values.

There is an ongoing debate over the placement of microphones at ground or off-ground locations for measuring and characterizing jet noise. The American National Standards Institute/Acoustical Society of America (ANSI/ASA S12.75-2012) standard for measuring high-performance military jet aircraft dictates off-ground

placement of microphones for measuring tied-down aircraft emissions. Off-ground placement simulates the position of an observer’s ear and has been shown to provide cleaner data for measuring acoustic nonlinearities for some flyover measurements,¹⁰ although ground interference nulls the result in the spectra due to such placement.¹¹ Whereas there are methods to address ground interference effects,^{12,13} there are a number of studies that rely on acoustical data collected at ground-based arrays near full-scale military aircraft.^{14,15} Placement of microphones on the ground eliminates interference nulls but due to the immediate reflection at the microphone-surface interface, there is an increase in the measured pressure compared to a free-field measurement. In addition to increased pressure, increased $Sk\{\partial p/\partial t\}$ values have been observed at the ground relative to the air.¹⁶ The potential for nonlinear reflections of acoustic shocks at ground locations, however, has not been directly investigated in the context of jet noise.

There are a variety of classifications for nonlinear reflections. In 1878, Ernst Mach first classified shock wave reflections as either regular or irregular.¹⁷ Regular reflections (RRs) consist of two shocks, an incident and a reflected shock, as seen in Fig. 1(a). The amplitudes and angles of incidence relative to the surface of the incident and reflected shocks can differ slightly for RR and do not follow the linear reflection described by the Snell-Descartes law. In addition to the incident and reflected shocks, irregular reflections (IRs) have a third shock, called the Mach stem, which travels parallel to the surface as shown in Fig. 1(b). Mach stem formation is caused by changes in the medium induced by the incident shock causing the reflected shock to travel faster than and coalesce with the incident

^{a)}This paper is part of a special issue on Supersonic Jet Noise.

^{b)}Electronic mail: aaron.burton.vaughn@gmail.com, ORCID: 0000-0002-5569-9694.

^{c)}ORCID: 0000-0003-4868-3114.

^{d)}ORCID: 0000-0002-5768-6483.

^{e)}ORCID: 0000-0001-8531-2051.

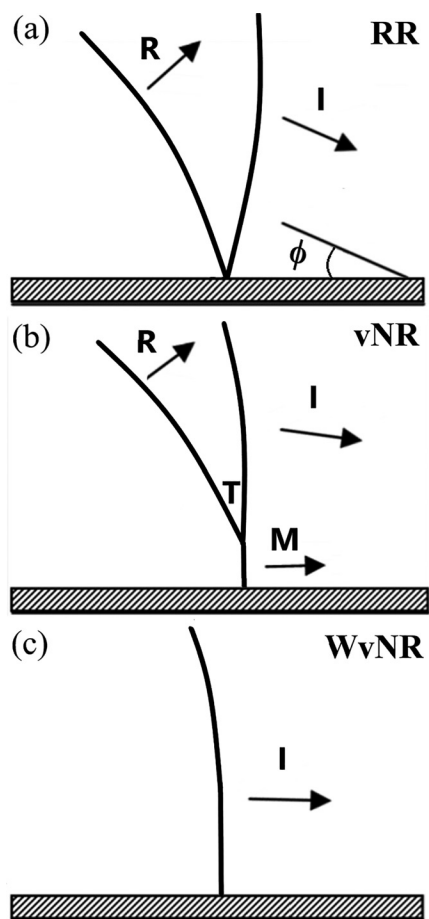


FIG. 1. (a) Regular reflection (RR), (b) vNR, and (c) WvNR schematics (similar to Fig. 3 in Ref. 24, Fig. 1 in Ref. 25, and Fig. 1 in Ref. 35).

shock. The intersection of the three shocks in an IR is called the triple point. Although there are several subsets of IR that are based on the shock strength or flow deflection processes,^{18,19} for weak shocks (shocks with an acoustic Mach numbers below 0.47),²⁰ there are two types of IRs, von Neumann reflection (vNR) and weak von Neumann reflection (WvNR). These shock reflection types are named for the von Neumann paradox,^{21,22} which is the inability of von Neumann's three-shock theory²³ to predict IRs for weak shocks. Unlike IRs for strong shocks (called Mach reflections¹⁹), which have a slope discontinuity at the triple point, vNR have no slope discontinuity between the Mach stem and the incident shock as visualized in Fig. 1(b). Only a single, incident shock results for WvNR because the shock is at grazing incidence with the surface as pictured in Fig. 1(c).²⁴

The pressure amplitude at the ground due to the Mach stem of an IR is greater than that for a linear reflection. Two-dimensional simulations of shocks reflecting on a rigid boundary, performed by Desjoux *et al.*,²⁵ showed the pressure amplitude ratio approaching a factor of 2.5 for the three-shocks regime as opposed to doubling in the linear two-shocks regime described by Snell-Descartes laws. The one-shock regime for WvNR is expected to have less than a doubling of pressure.²⁶ Marchiano *et al.*²⁷ experimentally validated the pressure ratio increasing by a factor of 2.5 for

the Mach stem of vNR of weak shock waves in water. If the shocks in a jet noise waveform undergo a nonlinear, IR at the ground and their pressure ratio increases by a factor greater than two, whereas the remainder of the waveform increases by a factor of 2, it is hypothesized that there would be characteristic differences between the waveforms measured at the ground and those measured in the air: the ground waveform would have a higher ratio of energy contained in the shocks compared to the overall energy and, thus, may affect the perception of crackle.

Generally, experimental identification of the shock reflection type is performed by imaging the shock reflection pattern using techniques such as Schlieren^{22,27-29} and shadowgraphy.^{19,30} However, because shocks were not visualized directly for reflection identification during the jet noise measurements, potential shock reflection types are identified using a parameter based on measured shock characteristics. Based on theory and validated by experimental results, a critical parameter, a , has been proposed to bound the regime for a given shock reflection classification.²⁶ The critical parameter originates from the application of boundary conditions on the Khokhlov-Zabolotskaya equation³¹ and is defined as

$$a = \frac{\sin \phi}{\sqrt{2\beta M_a}}, \quad (1)$$

where ϕ is the angle of incidence relative to the ground [see Fig. 1(a)], β is the coefficient of nonlinearity of the propagation medium, given as $\beta = (\gamma + 1)/2$, γ is the ratio of specific heat of the medium, and M_a is the acoustic Mach number. Physically, the acoustic Mach number is the ratio of the maximum particle velocity at the shock to the ambient sound speed in the medium but can be calculated using pressure measurements as follows:

$$M_a = \frac{\Delta P}{\gamma P_{\text{atm}}}, \quad (2)$$

where ΔP is the pressure change over the shock, P_{atm} is the atmospheric pressure, and γ is the ratio of the specific heat of the medium.²⁶ For a given medium, the critical parameter value depends only on the angle of incidence and acoustic Mach number. For weak acoustic shocks or N -waves, Baskar *et al.*²⁶ theoretically predicts $a = 0.4$ as the transition from WvNR to vNR and $a = 0.8$ as the transition from vNR to RR. Experimental validation by Karzova *et al.*²⁴ indicated transitions bounded at $a = 0.38$ and $a = 1.05$ for individual shock pulses where $M_a = 0.044$ and transitions at $a = 0.58$ and $a = 1.1$ for shocks where $M_a = 0.006$. Similarly, Marchiano *et al.*²⁷ indicated the transitions at $a = 0.36$ and $a = 0.91$ for ultrasonic pulses in water. Leete *et al.*³² studied gaseous explosions reflecting over a hard ground and found that the transition point from RR to IR occurred at $a > 0.8$, although they observed a discontinuity between the Mach stem and incident shock, suggesting that the transition occurred while the shock strength was

sufficient to generate a Mach reflection. Represented in M_a - ϕ space, Fig. 2 shows the transitional critical parameter values used in this study: $a = 0.4$ as the transition between WvNR and vNR and both $a = 0.8$ and $a = 1.1$ as the transition between vNR and RR from the theoretical and experimental results. The transition at $a = 0.4$ for WvNR and vNR is theoretically predicted and validated by experiments with similar M_a values to the shocks in the present study. It is anticipated that the transition from RR to vNR occurs at $a > 0.8$, but due to lack of visual confirmation, the two a values are used to bound the maximum a value for potential occurrences of vNR based on the theoretical prediction and experimental findings.

The goal of this paper is to identify differences between ground and off-ground jet noise measurements and provide evidence for the occurrence of irregular shock reflections as a partial explanation for these differences. In order to calculate the critical parameter, a , to predict the shock reflection type for an ensemble of shock events, the acoustic Mach number and angle of incidence for each event is determined. An explanation of the acoustic Mach number calculation and the event-based beamforming method used to find the angle of incidence are first presented. Predictions of shock reflection type for shock-like events across the entire array are then provided, after which the percentage of shocks expected to undergo vNR are discussed in relationship to elevated $Sk\{\partial p/\partial t\}$ values.

II. MEASUREMENT

This study examines acoustical data collected near a tied-down high-performance military aircraft using a linear array of ground-based microphones as depicted in Fig. 3(a). The array consisted of 71 G.R.A.S. 1/4 in. type 1 microphones (Copenhagen, Denmark) located 8–10 m from the estimated jet shear layer and spanned 32 m with a 0.45-m inter-microphone spacing. Pressure waveforms were synchronously acquired using National Instruments PXI-449X cards (Austin, Texas) sampling at 204.8 kHz for at least 10 s for each of 5–6 run-ups at 75%–150% engine thrust request (ETR). Engine conditions greater than 100% ETR are due to

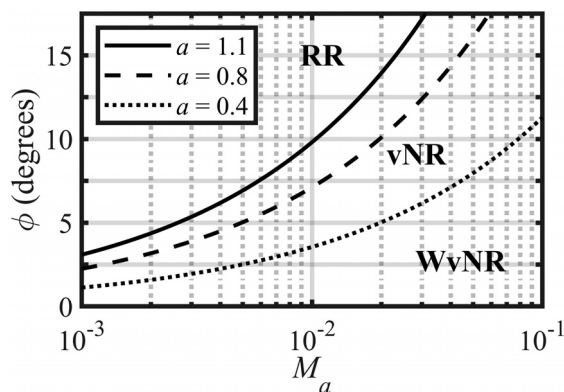


FIG. 2. Shock reflection classification in M_a - ϕ space based on transitional critical parameter values.

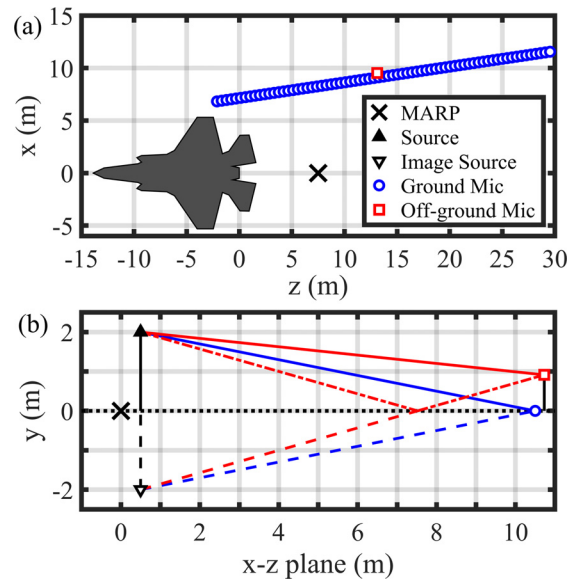


FIG. 3. (Color online) (a) Schematic of tied-down high-performance military aircraft and a ground-based linear microphone array, and (b) direct and reflected propagation paths for the off-ground microphone with an assumed source at the jet nozzle lip line, $(x, y) = (0.5, 2)$ m, at the downstream distance of the MARP, $z = 7.5$ m.

the addition of the afterburner. The coordinate system shown in Fig. 3(a) is set where x is the sideline distance, y is the height above the ground, z is the downstream distance, and the origin is at the point on the ground directly underneath the jet nozzle exit. The center of the nozzle was approximately 2 m off the ground. The microphone array reference point (MARP) is shown in Fig. 3(a) and was located 7.5 m downstream of the nozzle. The average atmospheric pressure across measurements was 93.5 kPa. More details for this measurement can be found in Ref. 4.

An additional microphone 0.91 m (3 ft) off the ground located near the ground array is denoted by a square in Fig. 3(a) and allows for a comparison between ground and off-ground shocks. The distance between the ground microphone (located at $z = 9.1$ m) and the off-ground microphone is 0.31 m in the x - z plane and 0.91 m in the y -direction as shown in Fig. 3(b). A 1.0-ms time delay is calculated for the path length differences between the direct and an assumed linear reflected path for the off-ground microphone by assuming a source at the jet nozzle lip line at the MARP downstream location $(x, y, z) = (0.5, 2.0, 7.5)$ m [see Fig. 3(b)].

The average $Sk\{\partial p/\partial t\}$ and overall sound pressure level (OASPL) across 5–6 run-ups at each engine condition are given in Fig. 4. For $z < 20$ m, the $Sk\{\partial p/\partial t\}$ follows a similar spatial trend across all engine conditions. However, for $z > 20$ m, trends diverge with larger $Sk\{\partial p/\partial t\}$ values occurring at lower engine conditions. The OASPL increases at all locations when engine conditions are increased from 75% ETR to 130% ETR. At the afterburner conditions, levels increase slightly across most of the array from 130% ETR to 150% ETR, except about the peak ($z = 8$ – 12) where levels are greatest for 130% ETR. The OASPL peak shifts upstream and broadens with the engine condition.

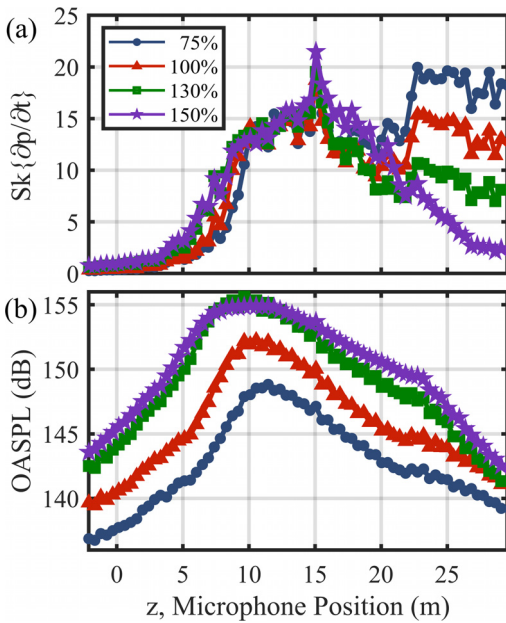


FIG. 4. (Color online) (a) Derivative skewness and (b) overall sound pressure level (OASPL) measurements along the ground array averaged across 5–6 runs at each engine condition.

Comparing OASPL and $Sk\{\partial p/\partial t\}$ peaks, the OASPL peaks are consistently upstream of the $Sk\{\partial p/\partial t\}$ peaks.

III. METHODS

Two event types of interest related to acoustic shocks are first defined. For each event, the acoustic Mach number and angle of incidence are determined so that the critical parameter can be calculated and used to predict the potential shock reflection type.

A. Shock characterization

The first event type of interest is defined by the 100 largest values of the derivative of the 10-s pressure waveform. This event definition selects the steepest portions of the waveform, which are the most likely candidates for IR. However, well-defined shocks may not exist at all locations along the array. Events are determined in the same manner as for those examined in an event-based beamforming process described in Ref. 33.

The second event type of interest is acoustic shocks identified using a criterion developed by Reichman *et al.*³ where an acoustic shock is defined by the value of the derivative of the pressure waveform exceeding 15 times the standard deviation of the derivative waveform ($15\sigma_{\partial p/\partial t}$). This statistical criterion differentiates the large derivative outliers that are common for shock waves from the other components of the jet noise. Although the criterion is sensitive to the sampling frequency, this dataset satisfies the sampling frequency requirement suggested by Reichman *et al.*³⁴ of at least 100 times the characteristic frequency, which is 100–200 Hz for most of the array.¹⁴

Values for the $15\sigma_{\partial p/\partial t}$ criterion and the resulting shock counts along the microphone array for four engine conditions are shown in Fig. 5. The use of the standard deviation normalizes the variation within a given waveform even though the criterion changes with the downstream position. Two spatial trends for the $15\sigma_{\partial p/\partial t}$ criterion are similar to OASPL trends in Fig. 4(b). First, as a function of the downstream distance, the values increase, peak at $z \approx 10$ m, and then decrease along the array at all engine conditions. Second, as a function of the engine power, the values increase from 75% ETR to 130% ETR and then have similar values at the two afterburner conditions (130% ETR and 150% ETR). This suggests that the large derivative values increase with increases in the amplitude. Interestingly, for $z > 20$ m, the $15\sigma_{\partial p/\partial t}$ criterion converges to having nearly identical values at all engine conditions.

Whereas the shock criterion identifies a number of shocks in the majority of channels along the ground array as shown in Fig. 5(b), there are locations at $z < 5$ m that have no shock counts. On the other hand, if the time waveform is sufficiently steep and sampled fast enough, multiple samples tracking the pressure rise of a shock may satisfy the $15\sigma_{\partial p/\partial t}$ criterion. Therefore, caution is needed to make certain that shocks are not double counted. The spatial trend across the entire array of shock counts is similar to the $Sk\{\partial p/\partial t\}$ trend shown in Fig. 4(a). This is particularly interesting for $z > 20$ m where the shock counts increase with decreasing engine powers. The use of the first event type (the top 100 largest derivatives) is justified by it, providing a means to examine the potential for nonlinear reflections across the entire array, even though there are no shocks identified by the $15\sigma_{\partial p/\partial t}$ shock criterion at upstream locations. Irregular shocks are not expected where there are no shock counts, according to the shock criterion. It is anticipated that these

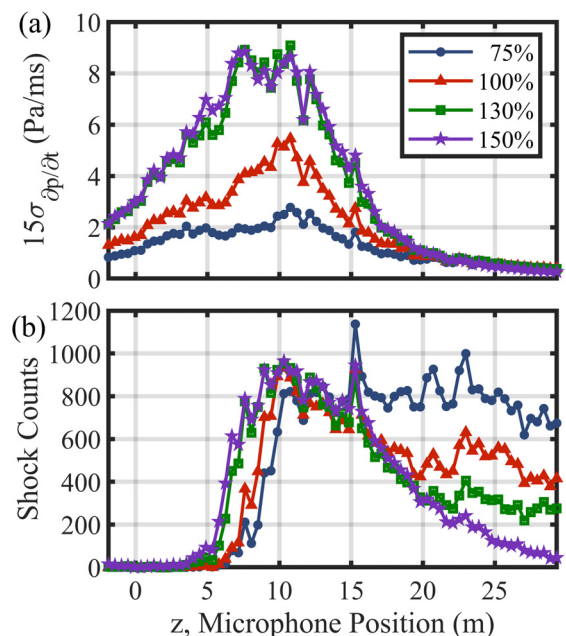


FIG. 5. (Color online) (a) Shock criteria of $15\sigma_{\partial p/\partial t}$ and the (b) shock counts along the microphone array.

non-shock events would fall into the RR classification, although they may actually be linear reflections as only shocks may be characterized using shock reflection classifications.

B. Shock strength

To represent the shock strength, this study utilizes the acoustic Mach number, M_a , as defined in Eq. (2). There are other viable metrics, such as the pressure ratio, density ratio, or shock Mach number, that could be used to characterize shock strength. The use of M_a in Eq. (1) motivates the choice of M_a to quantify the shock strength in this study. An example waveform segment in Fig. 6 is marked with a derivative event and upper (P_2) and lower (P_1) peak pressures, which are used to calculate M_a . Because shocks are defined within continuous noise, $\Delta P = P_2 - P_1$ rather than being equal to P_2 as would be the case for a single shock event in a quiescent environment.

C. Angle of incidence

The method to determine the angle of incidence, ϕ , is similar to the event-based beamforming procedure described in Ref. 33 and visually depicted in Fig. 7. First, a two-point cross correlation is performed to determine the propagation angle, ψ , for an event of interest. For each event defined in the upstream channel of the 70 adjacent microphone pairs, a 20-ms Hann window is applied about the large derivative or shock event. Then, the event is compared with a similarly windowed waveform segment recorded by the adjacent downstream microphone. The window was chosen to be long enough to obtain a meaningful cross correlation but short enough to isolate the energy of just the shock and not that of the underlying jet noise. From the cross correlation between the two windowed waveform segments, a time lag, τ , is calculated. Assuming the shock wave is locally planar and travels at the speed of sound, c , a distance of $c\tau$ forms a right triangle with the inter-microphone spacing, d , as the hypotenuse (see Fig. 5 in Ref. 33). The event’s propagation angle, ψ , relative to the microphone array (see Fig. 7), is then calculated as

$$\cos \psi = \frac{c\tau}{d}. \tag{3}$$

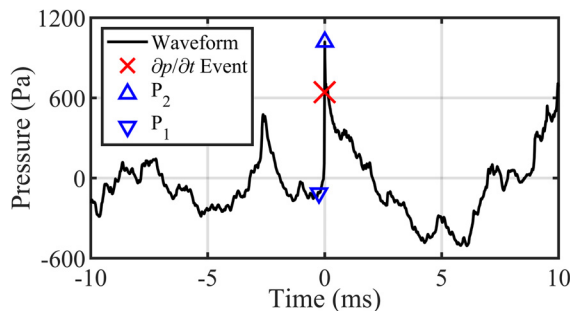


FIG. 6. (Color online) Example waveform segment of a large derivative event with the upper and lower peak pressures noted.

Next, the apparent origin of the event is determined along the jet lip line located at $(x, y) = (0.5, 2)$ m. Although the shock may originate at the shear layer, a different height, or any point along the path, the jet lip line is used in congruence with the previously performed event-based beamforming study in Ref. 33. With a vertex at the microphone pair midpoint, a vector \vec{r}_s extending toward the source, and a vector \vec{r}_m extending along the microphone array, the formula for an angle between two vectors is given in Eq. (4) and used to solve for the z -component of the vector \vec{r}_s .

$$\cos \psi = \frac{\vec{r}_m \vec{r}_s}{|\vec{r}_m| |\vec{r}_s|}. \tag{4}$$

Now, taking the path length, $|\vec{r}_s|$, and the source height, h , the angle of incidence, ϕ , shown in Fig. 7 is calculated as

$$\phi = \sin^{-1} \left(\frac{h}{|\vec{r}_s|} \right). \tag{5}$$

The grazing incidence is 0° and the normal incidence is 90° for ϕ in this orientation. This process is repeated for each event, resulting in a unique (M_a, ϕ) pair and a value for each event.

IV. GROUND AND OFF-GROUND SHOCK COMPARISONS

Before examining the results for the shock reflection classifications of the events of interest, differences are presented for shocks measured at a single, closely located ground and a single, closely located off-ground location. Discrepancies between ground and off-ground measurements in $Sk\{\partial p/\partial t\}$ values may exist due to the presence of nonlinear ground reflections. To aid in the comparison of the ground and off-ground measurements, a waveform is generated with a simulated linear ground reflection. This is done by adding the ground measurement waveform to itself with a 1-ms time delay, which corresponds to the path length difference between the direct and reflected path for the off-ground microphone as visualized in Fig. 3(b). The pressure of the simulated-ground-reflection waveform is

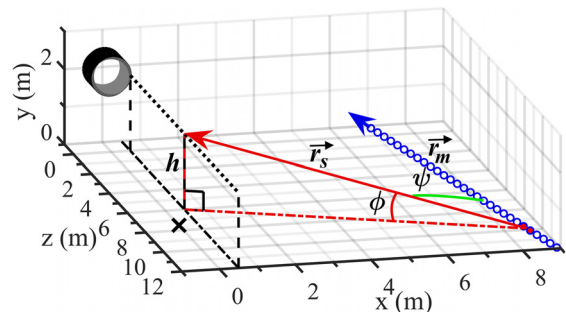


FIG. 7. (Color online) Beamforming schematic of the angle of incidence, ϕ , with the propagation angle, ψ , relative to the ground array of microphones noted as circles, the jet nozzle represented by a cylinder, and the MARP marked by a “x.”

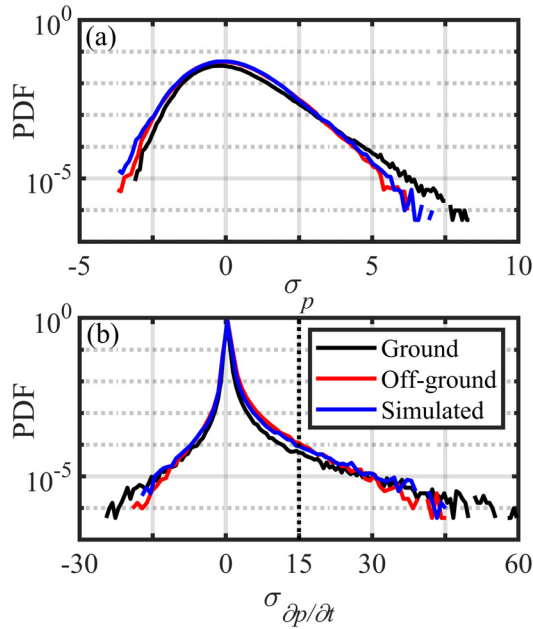


FIG. 8. (Color online) Probability density functions (PDFs) of the (a) pressures and (b) time-derivative pressures for ground, off-ground, and simulated waveforms at 150% ETR. The vertical dotted line in (b) indicates the shock criterion of $15\sigma_{\partial p/\partial t}$.

then halved so that the OASPL of the simulated waveform is similar to that of the off-ground measurement.

Probability density functions (PDFs) of the pressures and time-derivative pressures for the ground, off-ground, and simulated cases at 150% ETR are provided in Fig. 8. Each distribution is normalized by its respective standard deviation, and the logarithmic scaling on the ordinate allows for inspection of the distribution tails, which are the drivers of the skewness value due to its cubic nature. The pressure skewness ($Sk\{p\}$) and derivative skewness ($Sk\{\partial p/\partial t\}$) averaged across five run-ups at 150% ETR are noted in Table I. The pressure distribution for the simulated waveform in Fig. 8(a) approaches that of the off-ground measurement, although the $Sk\{p\}$ values are underpredicted. This suggests that a linear reflection may generally account for the differences in the $Sk\{p\}$ values for ground and off-ground measurements. The $Sk\{\partial p/\partial t\}$, on the other hand, is greater for the simulated waveform than is measured off-ground (see Table I). Whereas this demonstrates that the $Sk\{\partial p/\partial t\}$ value decreases for a linearly simulated reflection compared to a ground measurement, the $Sk\{\partial p/\partial t\}$ is still significantly greater than the off-ground measurement. This partly may be attributed to the ground waveform

TABLE I. Averaged derivative skewness, pressure skewness, shock criteria, shock counts per second, and average maximum shock derivative values across five runs for 150% ETR at a single location.

Case	$Sk\{p\}$	$Sk\{\partial p/\partial t\}$	$15\sigma_{\partial p/\partial t}$ (Pa/ms)	Shocks/s	$\langle\sigma_{\partial p/\partial t}\rangle_{\max}$
Ground	0.70	15.9	6.7	86.6	$25.9 \sigma_{\partial p/\partial t}$
Off-ground	0.41	9.5	4.4	97.8	$20.4 \sigma_{\partial p/\partial t}$
Simulated	0.36	11.2	4.8	97.4	$22.9 \sigma_{\partial p/\partial t}$

containing nonlinear reflections that inherently cause the simulated waveform to contain stronger shocks than observed at the off-ground location.

Further shock comparisons are made with the application of the $15\sigma_{\partial p/\partial t}$ shock criterion, shown by a vertical dotted line in Fig. 8(b). These include the $15\sigma_{\partial p/\partial t}$ values, shock counts, and averaged derivative values of the events exceeding the $15\sigma_{\partial p/\partial t}$ criterion, $\langle\sigma_{\partial p/\partial t}\rangle_{\max}$ as noted in Table I for 150% ETR. A linear superposition of a delayed shock-containing waveform with itself might suggest that there would be a doubling of shock counts; however, there are, on average, only 12% more shock counts for the off-ground and simulated waveforms relative to the ground measurement. Fewer shocks at the ground measurement location suggest that there is a fundamental difference in the type or strength of shocks at the ground versus off-ground location that causes an increase in $Sk\{\partial p/\partial t\}$ values at the ground. The average maximum shock derivative, $\langle\sigma_{\partial p/\partial t}\rangle_{\max}$, is greater at the ground than off-ground, suggesting that the shocks measured at the ground are, on average, steeper, which would be the case for nonlinear reflections. In addition to this, the pressure ratio of the average peak pressure for the shocks at the ground relative to the off-ground measurement is 2.3. This increase in pressure matches the predicted increase in the pressure ratio by Desjoux *et al.*²⁵ for IRs and the value approaches the factor of 2.5, observed by Marchiano *et al.*,²⁷ for irregular shock reflections in water.

V. RESULTS FOR THE LARGEST 100 DERIVATIVE EVENTS

The ground versus off-ground shock analysis presented evidence for stronger shocks at the ground. Here, the assertion is reinforced that stronger shocks could be due to nonlinear reflections. The feasibility of IRs occurring is examined for the top 100 largest derivative events at each of the 70 microphone pairs along the array. Histograms of spatial variations in acoustic Mach number and angle of incidence are examined for two engine conditions: 75% ETR and 150% ETR. Results in the M_a - ϕ space are then presented for shock reflection classification. To further analyze the shock reflection classification, critical parameter value histograms are presented as a function of the microphone position. Average values across the top 100 largest derivative events are then used for subsequent comparisons across engine conditions.

A. Acoustic Mach number and incidence angle histograms

The occurrences of M_a values for the top 100 largest derivative events at each of the 70 microphone pairs are given for 75% ETR and 150% ETR in Fig. 9. The abscissa is the z-coordinate of the microphones in the array pictured in Fig. 3, and the ordinate is the array of histogram bins of M_a values calculated for each event in 0.001 increments. The shading represents the number of event counts in each

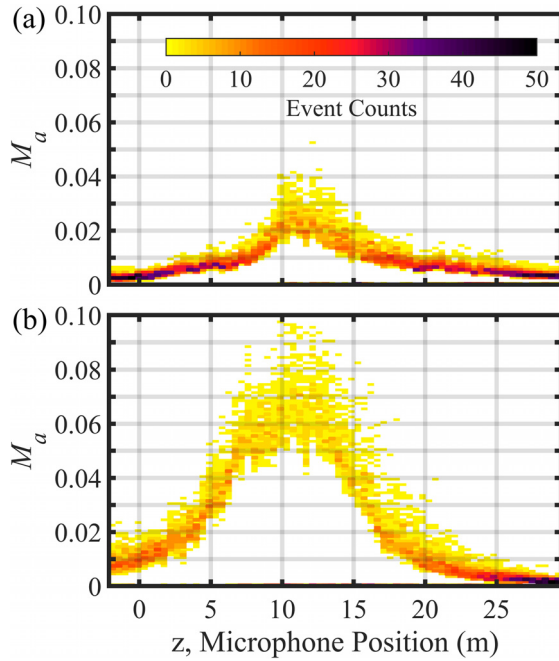


FIG. 9. (Color online) Histograms of acoustic Mach numbers, M_a , for the top 100 largest derivative events across each microphone pair for (a) 75% ETR and (b) 150% ETR.

histogram bin. Each vertical slice corresponds to a microphone pair for which the sum of the binned event counts is 100. Both engine conditions contain a peak at $z = 10\text{--}13$ m, similar to the OASPL shown in Fig. 4(b). At 150% ETR, the peak is broader and the M_a values are nearly double that of 75% ETR. At either end of the microphone array ($z < 3$ m and $z > 22$ m), the M_a values for both engine conditions are similar. However, the M_a values are, on average, greater for $z < 3$ m and lower for $z > 22$ m at 150% ETR.

Figure 10 depicts, in the same format as Fig. 9, the angle of incidence, ϕ , calculated via the method in Sec. III C, for the events along the microphone array. The abscissa is the same as that in Fig. 9 with the ordinate now representing histogram bins for angles of incidence in 0.25° increments. For both 75% ETR and 150% ETR, the maximum angle of incidence is approximately 15° and occurs at $z = 2\text{--}3$ m. The angles then incrementally decrease to 5° at the end of the array. However, the slope behaves differently for the two engine conditions. A steeper slope occurs for 75% ETR from $z = 3\text{--}20$ m and minimal reduction at $z > 20$ m. This contrasts with 150% ETR, which has a small drop in the angle of incidence for $z < 15$ m and a steeper slope for $z > 15$ m. Also, while the distributions are rather narrow for both cases, the distributions are broader for 150% ETR at $z < 5$ m and $z > 15$ m.

The overall trend is most likely influenced by the positioning of the array. The downstream microphone locations are farther away from the jet nozzle lip line, which increases the propagation path length [see \vec{r}_s in Fig. 7(b)] and results in smaller angles of incidence. Other differences in angles of incidence between the two engine conditions at a given microphone location are due to shocks having different

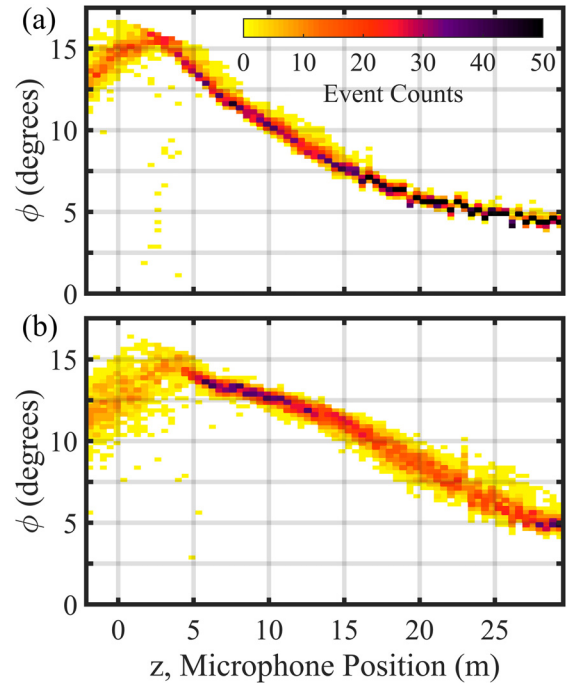


FIG. 10. (Color online) Histograms of angle of incidences, ϕ , for the top 100 largest derivative events across each microphone pair for (a) 75% ETR and (b) 150% ETR.

source locations. From the event-based beamforming results in Ref. 33, the source region for 75% ETR is more compact and predominantly upstream of the MARP, whereas the source region at 150% ETR is broader and extends downstream of the MARP.

B. M_a - ϕ space and critical parameter values

Figure 11 presents the top 100 derivative events from all microphone pairs in M_a - ϕ space for 75% ETR and 150% ETR. Dots represent individual shock events with the shading denoting the downstream microphone position. Reflection regimes are noted and bounded by the curved lines that indicate the transitional critical parameter value. For both engine conditions, 35% of the total 7000 events across the entire array fall into the $0.4 < a < 0.8$ vNR regime and about 60% fall into the $0.4 < a < 1.1$ vNR regime. Practically no events fall into the WvNR regime. The overall trend for events in M_a - ϕ space is smoothly varying with the downstream microphone position. The events with low M_a and large ϕ , located in the upper left corner of Fig. 11, are recorded at the upstream microphones. The distribution of events decreases in ϕ and increases in M_a with downstream microphone pair locations until the point along the array is reached with the peak OASPL (at $z \approx 10$ m). Then, M_a decreases again as ϕ continues to decrease toward the end of the array.

Spatial and quantifiable trends are more readily identifiable in Fig. 12, which shows the histograms of calculated a values for the top 100 derivative events at each microphone pair for 75% ETR and 150% ETR. The a values for the events at each microphone location were binned in 0.05

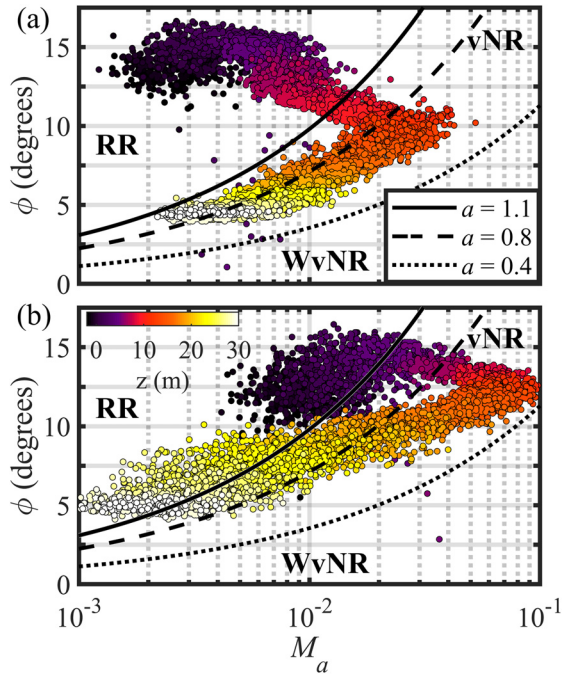


FIG. 11. (Color online) M_a - ϕ space results of the top 100 top derivative events for (a) 75% ETR and (b) 150% ETR with lines indicating the transitional critical parameter values and dot shading noting the microphone downstream position.

increments, and the horizontal lines represent the two transition criteria that separate the RR and vNR regimes and the one criterion separating the vNR and WvNR regimes. As previously stated, large derivative events that are not necessarily shocks may end up being classified as RR, although a linear reflection may be more appropriate.

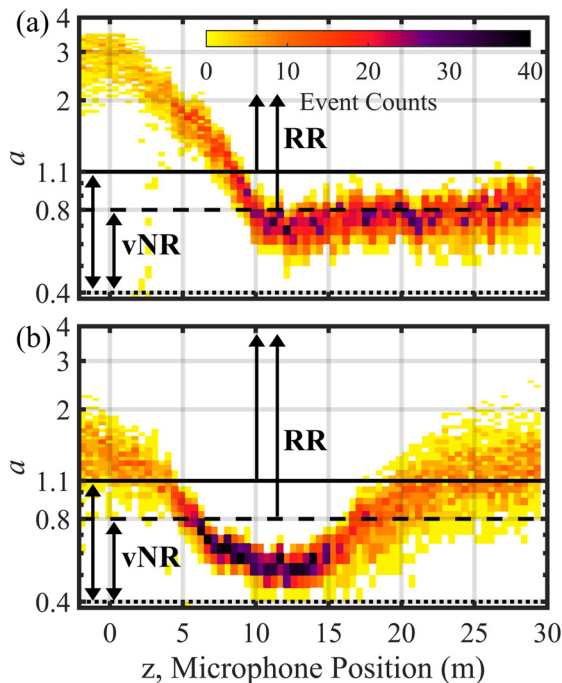


FIG. 12. (Color online) Histograms of critical parameter values for (a) 75% ETR and (b) 150% ETR.

The overall a trend differs for the two engine conditions in Fig. 12. For $z < 7$ m, the distribution spread varies significantly for both engine conditions with greater a values at 75% ETR. In the trough region from $z = 7$ –15 m, the distributions are the densest along the array. For $z < 15$ m, the distribution for 75% ETR remains moderately dense and centered about $a = 0.8$, whereas for 150% ETR, the a value increases and the distribution broadens, extending into the RR regime.

The distributions of the acoustic Mach number (see Fig. 9) and angle of incidence (see Fig. 10) directly impact the histograms of calculated a values and helps explain trends in Fig. 12. For $z < 7$ m, the larger angle of incidence and especially the lower acoustic Mach numbers for 75% ETR drive the a values into the RR region more so than for the 150% ETR. In the trough region from $z = 7$ –15 m, the angles decrease and acoustic Mach numbers increase sufficiently enough to transition the a values into the vNR region for both engine conditions. For $z > 15$ m, the angle of incidence and acoustic Mach number both decrease, causing 150% ETR to trend toward RR, whereas greater acoustic Mach numbers at 75% ETR keep it mostly in the vNR region. This means that the derivative events are more likely to be in the vNR regime at 75% ETR than at 150% ETR for far downstream locations, which may be a plausible explanation for the elevated $Sk\{\partial p/\partial t\}$ values at lower engine conditions in this downstream location (see Fig. 4).

C. Engine condition comparison

All four engine conditions are compared in M_a - ϕ space in Fig. 13(a). The mean of the 100 events for both the M_a and ϕ values at each microphone is taken. The use of more than 100 events would shift the mean value to the left in Fig. 13 due to a lower acoustic Mach number, whereas the angle of incidence is anticipated to vary minimally. The peak mean M_a is approximately 0.06, even though there are events in Fig. 9(a) in which M_a is approximately equal to 0.1 for 150% ETR. Similarly, for 75% ETR, the mean is less than that of the events with the greatest acoustic Mach number values that are most likely to be classified in the vNR regime. Nevertheless, the mean value of the top 100 derivative events transitions into the vNR regime for all four engine conditions. The acoustic Mach number drives the transition from RR to vNR (at $\phi > 10^\circ$) as each trend line predominantly crosses the boundary a line from left to right. The inclusion of 100% ETR serves as an intermediate case between 75% ETR and 150% ETR, whereas 130% ETR is nearly identical to 150% ETR.

Figure 13(b) shows the mean for the calculated a values versus the microphone pair position, which allows for spatial comparison of a values across the engine condition. In the upstream portion of the array, particularly $z > 5$ m, a values are greater in the RR regime for lower engine powers. The transition locations from RR to vNR occur farther upstream for greater engine powers and are reported in Table II. In the trough region from $z = 7$ –15 m, the a values

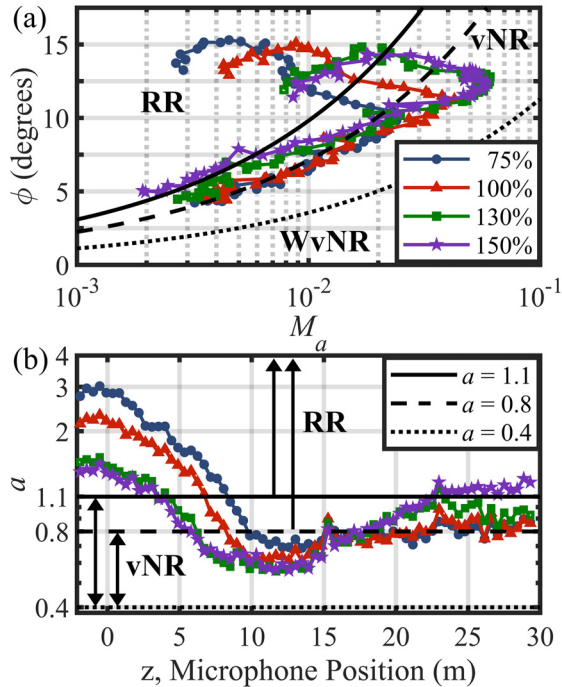


FIG. 13. (Color online) Averaged (a) M_a - ϕ space results and (b) critical parameter values for the top 100 derivative events for 75% ETR, 100% ETR, 130% ETR, and 150% ETR.

remain lower for higher engine powers. However, for $z > 18$ m, lower a values are observed for lower engine conditions. Whereas all engine conditions in the downstream region increase to at least $a = 0.8$, only 150% ETR transitions to $a > 1.1$. Differences at the end of the array are interesting as the shock strength generally would be assumed to increase with the engine condition, resulting in lower a values and IRs. Nevertheless, the jet noise directionality shifts toward the sideline at higher engine conditions⁴ and the propagation angle is greater due to an extended source. This results in ϕ and M_a values at the end of the array that are sufficient for greater a values at higher engine conditions and, therefore, the shocks are less likely to be classified in the vNR regime, even though levels are still greater at higher engine conditions.

D. Mach stem height

With the strong likelihood of vNR occurring in jet noise at nearby ground measurements, the Mach stem height is

TABLE II. Predicted transition locations from RR to vNR along the array for the mean a values of the top 100 derivative events at each engine condition based on the experimental ($a = 1.1$) and theoretical ($a = 0.8$) transitional critical parameter values.

ETR	z (m)
75%	8.4–9.8
100%	6.8–8.3
130%	3.5–6.2
150%	3.5–5.8

now considered for their potential impact on off-ground measurements. The Mach stem height, h_M , is expected to increase with the propagation distance, which corresponds to lower angles of incidence that drive the a value lower. When a decreases, h_M increases. Desjoux *et al.*²⁵ developed a relationship between h_M and a . This relationship resulted from a parametric numerical study of over 2000 configurations of varying spark source heights, propagation distances, and incident pressures. The equation is

$$h_M = h_s \left(\frac{\zeta}{a} \right)^2, \tag{6}$$

where h_s is the source height and ζ is a constant equal to 0.41 for which a physical meaning was not initially established, although it appears to be associated with the transition from vNR to WvNR at $a = 0.4$. Equation (6) predicts h_M to be less than h_s in the vNR regime. The application of Eq. (6) to the present study suggests $h_M = 0.28$ m for $a = 1.1$ and $h_M = 0.53$ m for $a = 0.8$, which are lower than the prescribed microphone heights in the ANSI/ASA standard. Karzova *et al.*³⁵ observed Mach stem heights that were in strong agreement with Eq. (6) while using the same spark source as in the Desjoux *et al.*²⁵ study; however, the source heights for the two studies ranged from 2 to 40 mm. This raises the question of whether the differences in the source type and scaling of source height allow for the application of Eq. (6) to the present study. Future investigation to determine the height of the Mach stems for vNR in jet noise is necessary to understand the potential impact of IRs impacting off-ground measurements.

VI. RESULTS FOR ALL SHOCKS

Section V established that there are events over a significant portion of the array predicted to be in the vNR regime. The present section now considers all shock events as defined by the $15\sigma_{\partial p/\partial t}$ criterion. These shocks are used to determine the percentage of shocks expected to undergo vNR and their relationship to increased $Sk\{\partial p/\partial t\}$ values. A brief discussion is also provided for the appropriate a value to bound the transition from RR to vNR.

The percentage of shocks along the ground array predicted in the vNR regime according to the experimentally ($0.4 < a < 1.1$) and theoretically ($0.4 < a < 0.8$) proposed bounds are given in Figs. 14(a) and 14(b), respectively. The percentage of shocks in the vNR regime are only reported for $z > 5$ m in Fig. 14 as there are no significant shock counts at $z < 5$ m [see Fig. 5(b)]. Whereas there is a substantial percentage of shocks across the array for the experimentally proposed vNR regime ($0.4 < a < 1.1$), there is a lower percentage for the theoretical case ($0.4 < a < 0.8$) because it is more restrictive. For $z < 15$ m, higher engine powers have a larger percentage of shocks that are predicted to be in the vNR regime with practically identical percentages at afterburner conditions (130% ETR and 150% ETR). However, for $z > 17$ m, the trend with the engine condition

flips with lower engine powers having a greater percentage of shocks in the vNR regime. This inverse relationship between the engine condition and percent of shocks in the vNR regime is similar to the relationship for the engine condition and $Sk\{\partial p/\partial t\}$ at the far downstream portion of the array.

The occurrence of vNR for a substantial percentage of shocks may help explain the increased $Sk\{\partial p/\partial t\}$ values along the ground array relative to off-ground measurements. There is a similar trend between the shock counts shown in Fig. 5(b) and $Sk\{\partial p/\partial t\}$ shown in Fig. 4(a), even at $z > 20$ m where there are greater values at lower engine conditions. Despite this trend between shock counts and $Sk\{\partial p/\partial t\}$ along the ground array, a similar number of shock counts at the ground and off-ground locations in Sec. IV have drastically different $Sk\{\partial p/\partial t\}$. This suggests that the shocks at the ground are stronger, which the occurrence of vNR supports, and the number of shock counts alone are not sufficient to quantify a relationship to $Sk\{\partial p/\partial t\}$. With a notable percentage of shocks in the vNR regime across the entire array, the subsequently increased amplitude ratio and shock steepness are likely to increase $Sk\{\partial p/\partial t\}$ values relative to the off-ground measurements that have no nonlinear reflections present.

The larger percentage of shocks in the vNR regime at lower engine powers for $z > 20$ m is given as a percentage increase relative to 150% ETR in Table III. Not only are there more shock counts at $z > 20$ m for the lower engine powers, a larger percentage of those shocks are predicted to be in the vNR regime. This is especially true for the experimental transitional critical parameter bounds.

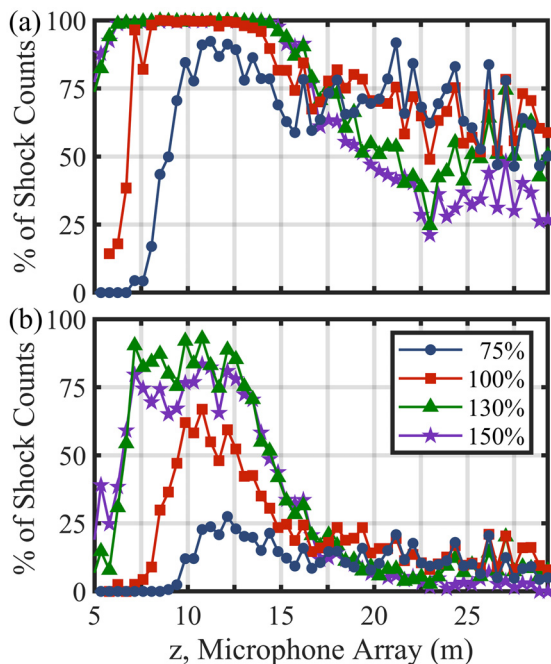


FIG. 14. (Color online) Percentage of shocks predicted to be vNR according to the (a) experimentally ($0.4 > a > 1.1$) and (b) theoretically ($0.4 > a > 0.8$) proposed bounds.

TABLE III. Average percentage increase in vNR shocks compared to 150% ETR at $z > 20$ m for the experimental ($0.4 < a < 1.1$) and theoretical ($0.4 < a < 0.8$) transitional critical parameter bounds.

ETR	$0.4 < a < 1.1$	$0.4 < a < 0.8$
75%	29.4%	6.1%
100%	27.5%	8.3%
130%	13.5%	3.9%

The relationship between the percentage of shock counts classified as vNR and the $Sk\{\partial p/\partial t\}$ value may lend insight into a potentially appropriate critical parameter value for the transition from RR to vNR. Throughout this study, two critical parameter values ($a = 0.8$ and $a = 1.1$) have been used to predict the transition from RR to vNR. Without a setup to visualize the shocks and confirm the appropriate shock reflection classification, the a value for the transition from RR to vNR must be determined indirectly. The results of this study suggest that a critical parameter value approaching $a = 1.1$ may be appropriate for characterizing the transition from RR to vNR for shocks embedded in jet noise. One piece of supporting evidence for this is that the percent increase in Table III for $0.4 < a < 1.1$ more closely following the observed trend of $Sk\{\partial p/\partial t\}$ increasing with the lower engine conditions. Also, with a less restrictive a value, there are more shocks undergoing vNR, which would further help explain the increase in $Sk\{\partial p/\partial t\}$ along the ground array. Thus, $a = 1.1$ is recommended until further evidence arises.

VII. CONCLUSION

This study has investigated the possibility of nonlinear shock reflections occurring for acoustic shocks in jet noise at ground-based measurements near a tied-down military aircraft. The nonlinear reflections are likely IRs of the von Neumann type. A comparison between measurements at a single ground and nearby off-ground location revealed that although there are a similar number of shocks as defined by the $15\sigma_{\partial p/\partial t}$ shock criterion, the resulting $Sk\{\partial p/\partial t\}$ values were 1.8 times greater at the ground for 150% ETR. The average maximum derivative of the shocks are $26\sigma_{\partial p/\partial t}$ at the ground compared to only $21\sigma_{\partial p/\partial t}$ off the ground, suggesting that the shocks measured at the ground are, on average, steeper. In addition, the shock pressure amplitude ratio at the ground relative to the off-ground is a factor of 2.3, which is greater than a linear doubling and a characteristic of IRs. This suggests that the increased $Sk\{\partial p/\partial t\}$ values of ground-based measurements near a military aircraft may be due to IRs, which may exaggerate crackle perception relative to nearby off-ground microphones.⁹

To predict shock reflection classification, the critical parameter, a , is calculated from the acoustic Mach number and angle of incidence for each shock. Examining the critical parameter values of the top 100 largest derivative events along the array reveals that vNR are expected primarily at locations where shocks are present as defined by the

$15\sigma_{\partial p/\partial t}$ criterion. The position along the array at which shocks transition from RR to vNR based on the experimental ($a = 1.1$) and theoretical ($a = 0.8$) critical parameter values occurs at $z = 3.5\text{--}9.8\text{ m}$ with the transition location occurring farther upstream for the greater engine powers. Examination of the critical parameter values of all of the shocks along the array defined by the $15\sigma_{\partial p/\partial t}$ criterion indicates that a substantial percentage of shocks are expected to exhibit vNR over the same extent of the array at which $\text{Sk}\{\partial p/\partial t\}$ values are significant. In addition to increasing the $\text{Sk}\{\partial p/\partial t\}$ compared to off-ground measurements along the majority of the ground array, IRs are a plausible explanation for increased $\text{Sk}\{\partial p/\partial t\}$ at the aft portion of the array where $\text{Sk}\{\partial p/\partial t\}$ increases with the lower engine power. Not only are there more shock counts at these aft locations, a larger percentage of the shocks is expected to be in the vNR regime. A critical parameter value approaching $a = 1.1$ may be an appropriate boundary between the RR and vNR regimes for shocks in jet noise. Additional investigation, including visualization of shock reflections in jet noise, is needed to develop quantitative relationships between the occurrence of IRs and the subsequent increase in $\text{Sk}\{\partial p/\partial t\}$ for ground measurements.

ACKNOWLEDGMENTS

The author gratefully acknowledges funding for the measurements provided through the F-35 Program Office and Air Force Research Laboratory. (Distribution A: Approved for public release; distribution unlimited, F-35 Public Affairs Office cleared 10/08/2020; JSF20-712.) This research was funded under an Air Force Research Laboratory Small Business Innovation Research program. The authors are also grateful for the reviewers' comments and feedback, which improved the content and clarity of this paper.

¹R. Fievet, C. E. Tinney, W. J. Baars, and M. F. Hamilton, "Coalescence in the sound field of a laboratory-scale supersonic jet," *AIAA J.* **54**(1), 254–265 (2016).
²P. Mora, N. Heeb, J. Kastner, E. J. Gutmark, and K. Kailasanath, "Effect of heat on the pressure skewness and kurtosis in supersonic jets," *AIAA J.* **52**(4), 777–787 (2014).
³B. O. Reichman, K. L. Gee, T. B. Neilsen, and S. H. Swift, "Acoustic shock formation in noise propagation during ground run-up operations of military aircraft," AIAA Paper 2017-4043, June (2017).
⁴M. M. James, A. R. Salton, J. M. Downing, K. L. Gee, T. B. Neilsen, B. O. Reichman, R. L. McKinley, A. T. Wall, and H. L. Gallagher, "Acoustic emissions from F-35 aircraft during ground run-up," AIAA Paper 2015-2375 (2015).
⁵K. L. Gee, V. W. Sparrow, M. M. James, J. M. Downing, C. M. Hobs, T. B. Gabrielson, and A. A. Atchley, "The role of nonlinear effects in the propagation of noise from high power aircraft," *J. Acoust. Soc. Am.* **123**(6), 4082–4093 (2008).
⁶S. H. Swift, K. L. Gee, and T. B. Neilsen, "Testing two crackle criteria using modified jet noise waveforms," *J. Acoust. Soc. Am.* **141**(6), EL549–EL554 (2017).
⁷J. E. Ffowes Williams, J. Simson, and V. J. Virchis, "Crackle": An annoying component of jet noise," *J. Fluid Mech.* **71**(2), 251–271 (1975).
⁸A. Krothapalli, L. Venkatakrishnan, and L. Lourenco, "Crackle—A dominant component of supersonic jet mixing noise," AIAA Paper 2000-2024, June (2000).

⁹K. L. Gee, P. B. Russavage, T. B. Neilsen, S. H. Swift, and A. B. Vaughn, "Subjective rating of the jet noise crackle percept," *J. Acoust. Soc. Am.* **144**(1), EL40–EL44 (2018).
¹⁰S. A. McInerney, K. L. Gee, J. M. Downing, and M. M. James, "Acoustical nonlinearities in aircraft flyover data," AIAA Paper 2007-3654, May (2007).
¹¹D. K. McLaughlin, C. W. Kuo, and D. Papamoschou, "Experiments on the effect of ground reflections on supersonic jet noise," AIAA Paper 2008-22, January (2008).
¹²K. L. Gee, T. B. Neilsen, and M. M. James, "Including source correlation and atmospheric turbulence in a ground reflection model for rocket noise," *Proc. Mtgs. Acoust.* **22**(1), 1–17 (2014).
¹³S. A. E. Miller, "The prediction of jet noise ground effects using an acoustic analogy and a tailored Green's function," *J. Sound Vib.* **333**(4), 1193–1207 (2014).
¹⁴T. B. Neilsen, A. B. Vaughn, K. L. Gee, S. H. Swift, A. T. Wall, J. M. Downing, and M. M. James, "Three-way spectral decompositions of high-performance military aircraft noise," *AIAA J.* **57**(8), 3467–3479 (2019).
¹⁵B. M. Harker, K. L. Gee, T. B. Neilsen, A. T. Wall, and M. M. James, "Source characterization of full-scale tactical jet noise from phased-array measurements," *J. Acoust. Soc. Am.* **146**(1), 665–680 (2019).
¹⁶M. B. Muhlestein, "Analyses of nonlinearity measures in high-amplitude sound propagation," Ph.D. dissertation, Brigham Young University, Provo, UT (2013), available at <https://scholarsarchive.byu.edu/etd/3994> (Last viewed 1 July 2020) (see Fig. 6.9 for $\text{Sk}\{\partial p/\partial t\} = 4$ at 48 kHz and p. 137 for peak $\text{Sk}\{\partial p/\partial t\} = 2.7$ in the NAH plane).
¹⁷E. Mach, "Über den Verlauf von Funkenwellen in der Ebene und im Raume" ("Over the course of radio waves in the plane and in space"), *Sitzungsbr. Akad. Wiss. Wien* **78**, 819–838 (1878).
¹⁸G. Ben-dor, *Shock Wave Reflection Phenomena* (Springer, New York, 2007), pp. 3–4 and 297–303.
¹⁹A. N. Semenov, M. K. Berezkina, and I. V. Krassovskaya, "Classification of pseudo-steady shock wave reflection types," *Shock Waves* **22**(4), 307–316 (2012).
²⁰G. Birkhoff, "Hydrodynamics: A study in logic, fact, and similitude," *Bull. Amer. Math. Soc.* **57**, 97–499 (1951).
²¹P. Colella and L. F. Henderson, "The von Neumann paradox for the diffraction of weak shock waves," *J. Fluid Mech.* **213**, 71–94 (1990).
²²B. W. Skews and J. T. Ashworth, "The physical nature of weak shock wave reflection," *J. Fluid Mech.* **542**, 105–114 (2005).
²³J. von Neumann, "Oblique reflection of shocks," in *John Von Neumann Collected Works*, edited by A. H. Taub (MacMillan, New York, 1963), Vol. 6, pp. 238–299.
²⁴M. M. Karzova, V. A. Khokhlova, E. Salze, S. Ollivier, and P. Blanc-Benon, "Mach stem formation in reflection and focusing of weak shock acoustic pulses," *J. Acoust. Soc. Am.* **137**(6), EL436–EL442 (2015).
²⁵C. Desjouis, S. Ollivier, O. Marsden, M. M. Karzova, and P. Blanc-Benon, "Irregular reflection of weak acoustic shock pulses on rigid boundaries: Schlieren experiments and direct numerical simulation on a Navier-Stokes solver," *Phys. Fluids* **28**(2), 1–14 (2016).
²⁶S. Baskar, F. Coulouvrat, and R. Marchiano, "Nonlinear reflection of grazing acoustic shock waves: Unsteady transition from von Neumann to Mach to Snell-Descartes reflections," *J. Fluid Mech.* **575**, 27–55 (2007).
²⁷R. Marchiano, F. Coulouvrat, S. Baskar, and J. L. Thomas, "Experimental evidence of deviation from mirror reflection for acoustical shock waves," *Phys. Rev. E* **76**(5), 1–5 (2007).
²⁸M. M. Karzova, T. Lechat, S. Ollivier, D. Dagna, P. V. Yuldashev, V. A. Khokhlova, and P. Blanc-Benon, "Effect of surface roughness on nonlinear reflection of weak shock waves," *J. Acoust. Soc. Am.* **146**(5), EL438–EL443 (2019).
²⁹M. Geva, O. Ram, and O. Sadot, "The non-stationary hysteresis phenomenon in shock wave reflections," *J. Fluid Mech.* **732**, R1–R11 (2013).
³⁰T. Suzuki, T. Adachi, and S. Kobayashi, "Experimental analysis of reflected shock behavior over a wedge with surface roughness," *JSME Int. J. Ser. B Fluids Therm. Eng.* **36**(1), 130–134 (1993).
³¹E. A. Zabolotskaya and V. R. Khokhlov, "Quasi-plane waves in the nonlinear acoustics of confined beams," *Sov. Phys. Acoust.* **15**, 35–40 (1969).
³²K. M. Leete, K. L. Gee, T. B. Neilsen, and T. T. Truscott, "Mach stem formation in outdoor measurements of shocks," *J. Acoust. Soc. Am.* **138**(6), EL522–EL 527 (2015).

- ³³A. B. Vaughn, K. L. Gee, S. H. Hales, K. M. Leete, A. T. Wall, J. M. Downing, and M. M. James, "Source localization of crackle-related events in military aircraft jet noise," *AIAA J.* (published online 2021).
- ³⁴B. O. Reichman, K. L. Gee, T. B. Neilsen, J. M. Downing, M. M. James, A. T. Wall, and S. A. McNerny, "Characterizing acoustic shocks in high-

- performance jet aircraft flyover noise," *J. Acoust. Soc. Am.* **143**(3), 1355–1365 (2018).
- ³⁵M. M. Karzova, T. Lechat, S. Ollivier, D. Dagna, P. V. Yuldashev, V. A. Khokhlova, and P. Blanc-Benon, "Irregular reflection of spark-generated shock pulses from a rigid surface: Mach-Zehnder interferometry measurements in air," *J. Acoust. Soc. Am.* **145**(1), 26–35 (2019).